

On the Energy Coupling from Magnetosonic Waves to High-Frequency Electromagnetic Ion Cyclotron Waves: Statistical Analysis

Kyungguk Min¹, Qianli Ma^{2,3}

¹Department of Astronomy and Space Science, Chungnam National University, Daejeon 34134, Korea.

²Department of Atmospheric and Oceanic Sciences, University of California, Los Angeles, CA, USA.

³Center for Space Physics, Boston University, Boston, MA, USA.

Key Points:

- Energy coupling from MS to high-frequency EMIC waves through low-energy proton heating is investigated using correlation analysis
- High-frequency EMIC wave occurrence correlates well with large anisotropy of 10–100 eV protons, required for the wave generation
- The correlation between low-energy protons and MS waves is rather poor, calling for alternative explanation for the origin of these protons

Abstract

In the inner magnetosphere, fast magnetosonic waves (MS waves) are known to resonantly interact with ring current protons, causing these protons to gain energy preferentially in the direction perpendicular to the background magnetic field. An anisotropic distribution of enhanced ring current protons is a necessary condition to excite electromagnetic ion cyclotron (EMIC) waves which are known to facilitate a rapid depletion of ultra-relativistic electrons in the outer radiation belt. So, when a simultaneous observation of high-frequency EMIC (HFEMIC) waves, anisotropic low-energy protons, and MS waves was first reported, a chain of energy flow from MS waves to HFEMIC waves through proton heating was naturally proposed. In this study, we carry out a statistical analysis using Van Allen Probes data to provide deeper insights into this energy pathway. Our results show that the occurrence of HFEMIC waves exhibits good correlation with the enhanced flux and anisotropy of low-energy protons, but the correlation between the low-energy protons and the concurrent MS waves is rather poor. The latter result is given support by quasilinear diffusion analysis, indicating negligible momentum diffusion rates at sub-keV energies, unless MS wave frequency gets very close to the proton cyclotron frequency (which constitutes only a small number of the cases). The fact that the first chain of the coupling is statistically inconclusive calls for an alternative explanation for the major source of the low-energy anisotropic proton population in the inner magnetosphere.

1 Introduction

Plasma waves are indispensable to the cross-energy and cross-species coupling in space plasmas. Fast magnetosonic waves (MS waves) in the inner magnetosphere resonantly interact with energetic ring current protons, causing these protons to gain energy preferentially in the direction perpendicular to the background magnetic field (e.g., Horne et al., 2000; Ma, Li, Yue, et al., 2019). An anisotropic distribution of enhanced ring current protons is the necessary condition to excite electromagnetic ion cyclotron (EMIC) waves (e.g., L. Chen, Thorne, Jordanova, Wang, et al., 2010) which are known to facilitate a rapid depletion of ultra-relativistic electrons in the outer belt (Usanova et al., 2014). So when a simultaneous observation of high-frequency EMIC (HFEMIC) waves, anisotropic low-energy protons, and MS waves by Van Allen Probes (Mauk et al., 2013) was first reported by Teng et al. (2019), a chain of energy flow from MS waves to HFEMIC waves through the heating of low-energy protons was naturally proposed (see Asamura et al., 2021, Figure 4). The HFEMIC waves in this event were different from typical ones in that the wave spectrum is narrow-banded ($\Delta f \lesssim 0.1f_{cp}$, where f_{cp} is the equatorial proton cyclotron frequency) and the peak frequency occurs at $\sim 0.95f_{cp}$ (Teng et al., 2019). According to linear theory (e.g., Kennel & Petschek, 1966; Teng et al., 2019), such HFEMIC waves resonantly interact with sub-keV protons (as opposed to 10–100 keV protons associated with typical EMIC waves) and requires temperature anisotropy ($A = T_{\perp}/T_{\parallel} - 1$) well exceeding the value (~ 1) associated with the excitation of typical EMIC waves (Yue et al., 2019; Jun et al., 2023). Indeed, the observation shows enhanced 90°-peaked (in pitch angle space) proton fluxes at energy $\lesssim 100$ eV, concurrent with HFEMIC activity (see Teng et al., 2019, Figure 1). Shortly, Asamura et al. (2021) reported a similar event detected by Arase (Miyoshi et al., 2018). Employing a technique called wave-particle interaction analysis that enables calculation of the Joule heating rate directly from wave and particle measurements, they presented compelling evidence for the proposed chain of energy flow.

Although it is often the case that the ring current proton populations accompany MS wave events (Ferradas et al., 2021; Wu et al., 2022) and several observational studies highlighted the ability of MS waves to energize them (Yuan et al., 2018; Ma, Li, Yue, et al., 2019; Hill et al., 2020), there is a growing body of work that questions the efficacy of MS wave-driven proton heating, particularly in the sub-keV range concerned here. In-

terestingly, Ferradas et al. (2021) showed that the majority of the H^+ and He^+ warm ion flux enhancement events are not associated with direct observation of these waves, although they did find that the flux enhancements and the pitch angle anisotropy in absence of MS waves were weaker. Wu et al. (2022) presented a correlation analysis between pancake pitch angle distributions of 10–300 eV protons and MS waves. Despite the conclusion (drawn purely based on the concurrent observation statistics) that MS waves contributed to the formation of low-energy anisotropic proton distribution, they noted that it is hard to justify this causal relationship from their diffusion analysis. Meanwhile, Min et al. (2022) analyzed the event of Teng et al. (2019) in detail to test the proposed energy coupling. They showed that while the observed 10–100 eV protons that exhibited large anisotropy are the likely source of the concurrent HFEMIC waves, the MS wave-driven heating becomes ineffective in the energy range relevant to this event, as far as the quasilinear process is concerned. On the other hand, Joseph et al. (2022) focused on the relation between MS waves and pitch angle anisotropy of warm ($\lesssim 500$ eV) protons by a case study. From a comparative analysis involving two nearly identical cases of pitch angle anisotropy of warm protons—one with concurrent MS waves and the other without them—and also from quasilinear theory, they concluded that MS waves are not responsible for the primary heating of these warm protons. Alternatively, they proposed that the recirculated polar wind plasma in the inner magnetosphere can cause the concurrent appearance of heated protons and MS waves.

As for the low-energy proton-to-HFEMIC link, there is no statistical analysis to draw a firm conclusion upon. Hence, in this study we carry out a statistical analysis using Van Allen Probes data to provide further insights into the energy pathway proposed by Teng et al. (2019) and Asamura et al. (2021). The aim of the study is (1) to help clear up the role of MS waves in the low-energy proton heating and (2) to evaluate whether the causal relation between HFEMIC waves and low-energy anisotropic protons is statistically supported. Our results show that while the occurrence of HFEMIC waves exhibits a good correlation with the enhanced flux and anisotropy of low-energy protons, the correlation between the key parameters of low-energy protons and concurrent MS waves is rather poor.

The present paper is organized as follows: Section 2 outlines the data and event selection. In Section 3, we investigate the causal relationship between HFEMIC waves and low-energy protons. This is followed by an investigation of the coupling between low-energy protons and concurrent MS waves in Section 4. Finally, Section 5 provides summary and discussion.

2 Data and Event Selection

The Van Allen Probes provide comprehensive plasma wave and particle measurements in the inner magnetosphere (Mauk et al., 2013). Here, we utilize the data obtained during the operation from 2013 to 2019. Observations of fields are from the Electric and Magnetic Field Instrument Suite and Integrated Science (EMFISIS; Kletzing et al., 2013, 2023). Specifically, we utilize the data from the fluxgate magnetometer which records the magnetic field at a maximum sampling rate of 64 Hz, and the waveform frequency receiver (WFR) that provides wave magnetic power spectra from 10 Hz to 12 kHz. The electric field data are provided by the electric fields and waves (EFW) instruments at a maximum sampling rate of 32 Hz (Wygant et al., 2013; Breneman et al., 2022) and used to identify low-harmonic MS waves. For low-energy protons, we utilize the data from the Helium Oxygen Proton Electron (HOPE) instrument of the Energetic Particle Composition and Thermal Plasma Suite which provides measurements of electrons and ions over the 1 eV to 50 keV energy range with full pitch angle coverage (Funsten et al., 2013; Spence et al., 2013). Finally, we use the background electron density data inferred from the upper hybrid resonance frequency (Kurth et al., 2015).

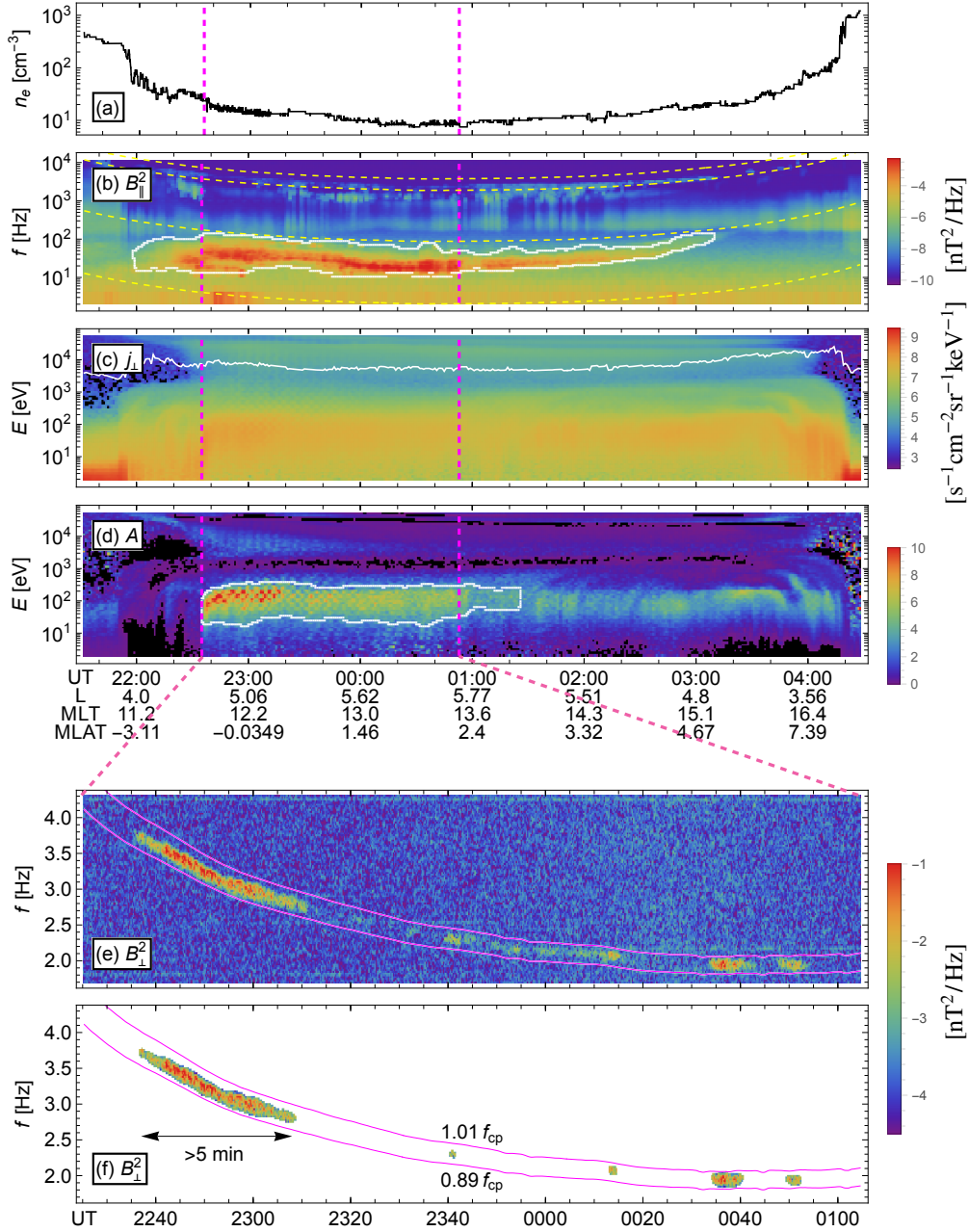


Figure 1. A sample event detected by Probe A on August 27, 2017. (a) Electron density inferred from the upper hybrid frequency. (b) The parallel component of the magnetic field spectrogram from WFR in units of nT^2/Hz . The yellow dashed curves running across the panel are f_{ce} , $0.5f_{ce}$, $\sqrt{1836}f_{cp}$ (approximate lower hybrid frequency), and f_{cp} , where f_{ce} and f_{cp} are the equatorial electron and proton cyclotron frequencies, respectively. The white outline demarcates automatically identified MS waves (see Section 4 for details). (c) Proton differential flux at 90° pitch angle in units of $\text{s}^{-1}\text{cm}^{-2}\text{sr}^{-1}\text{keV}^{-1}$. The white trace running across the panel denotes the Alfvén energy, $E_A = m_p v_A^2/2$, where $v_A = B_{eq}/\sqrt{4\pi m_p n_e}$ is the Alfvén speed. (d) Pitch angle anisotropy parameter, A , given by Eq. (1). The white outline demarcates the region of enhanced A (see Section 4 for details). (e) Perpendicular component of the magnetic field spectrogram in the HFEMIC wave frequency range, given in units of nT^2/Hz . The start and end of HFEMIC wave activity are denoted by the magenta vertical lines in panels (a-d). (f) HFEMIC waves identified by the automatic algorithm. The magenta curves denote 0.89 and $1.01f_{cp}$, respectively.

Because our main focus is the energy channel that gives rise to HFEMIC waves, we work with the events that specifically contain them. Figure 1 displays a sample event on August 27, 2017 where enhanced MS waves (Figure 1b) and low-energy ($\lesssim 1$ keV) protons (Figure 1c) occurred concurrently with HFEMIC waves (Figure 1e). Evident from the density profile of Figure 1a, not only HFEMIC waves (denoted by two vertical dashed lines) but also MS waves and low-energy proton enhancement were all found outside the plasmopause which is demarcated by the sudden drops in the density (one near 2200 UT on August 27 and another at 0430 UT on the following day). In addition to the flux enhancement, low-energy protons during this period also exhibited strong pitch-angle anisotropy, which will be described in detail in Section 3.

Considering that the number of events are small (Teng et al., 2019), we narrowed down candidate events first by visually inspecting magnetic field spectrograms. Although laborious, it was fairly straightforward to identify them visually because of the distinct characters of HFEMIC waves. While doing so, we also excluded the period where HFEMIC and typical EMIC waves appear simultaneously, and counted as one when two spacecraft with a small separation saw the same HFEMIC waves. We then generate boolean masks based on the criteria: (1) the sum of all three components of magnetic spectral power greater than $0.002 \text{ nT}^2/\text{Hz}$ and (2) frequency interval $0.89 < f/f_{cp} < 1.01$. We apply to each mask array a five-pixel Gaussian filter and label the values greater than 0.4 as HFEMIC waves. As an example, Figure 1f displays the identified HFEMIC wave signatures. Since there can be multiple patches of wave activity in one orbit, as the final step, we require that the longest blob in Figure 1f be at least five minutes long.

In the end, we found a total of 26 events. (The full list is tabulated in Supporting Information Table S3.) In comparison, a somewhat larger number of events (38 events) were found in Teng et al. (2019), who examined data from 2012 to 2018 based on a different set of criteria. Since the statistical properties of HFEMIC waves we have found (reproduced in Supporting Information S1 and S4) are consistent with those of Teng et al. (2019), our events can be regarded as a subset of theirs. We note that almost all HFEMIC events were found within 5° magnetic latitude and are associated with the electron plasma to cyclotron frequency ratio $f_{pe}/f_{ce} \lesssim 10$ which is the typical condition outside the plasmasphere. We also note that the increased sample size by reducing the minimum duration criterion did not change the fundamental conclusions of the present study due to the low occurrence of HFEMIC wave events.

3 HFEMIC Activity vs. Low-energy Protons

3.1 Correlation Analysis

To understand the source of HFEMIC waves, here we statistically examine low-energy protons during HFEMIC activity. In addition to elevated proton fluxes, pitch-angle anisotropy is an important parameter for HFEMIC wave growth. In fact, the case event examined by Teng et al. (2019, Figure 2b) exhibits a very anisotropic distribution in the sense that $T_\perp \gg T_\parallel$. To systematically measure the degree of anisotropy of low-energy proton distribution, we calculate the pitch angle anisotropy parameter (M. W. Chen et al., 1999; Li et al., 2009)

$$A(E_i) = \frac{\int_0^\pi j(E_i, \alpha) \sin^3 \alpha d\alpha}{2 \int_0^\pi j(E_i, \alpha) \cos^2 \alpha \sin \alpha d\alpha} - 1 \quad (1)$$

at every energy channel E_i , where j stands for the particle flux. Figure 1d displays this parameter for the sample event. Evidently, the enhancement of A is concurrent with the flux enhancement in the same energy range, which is markedly pronounced during the HFEMIC activity. Although not shown here, the corresponding pitch angle distribution in this energy range is sharply peaked at $\alpha = 90^\circ$, similar to Teng et al. (2019, Figures 1e and 1f).

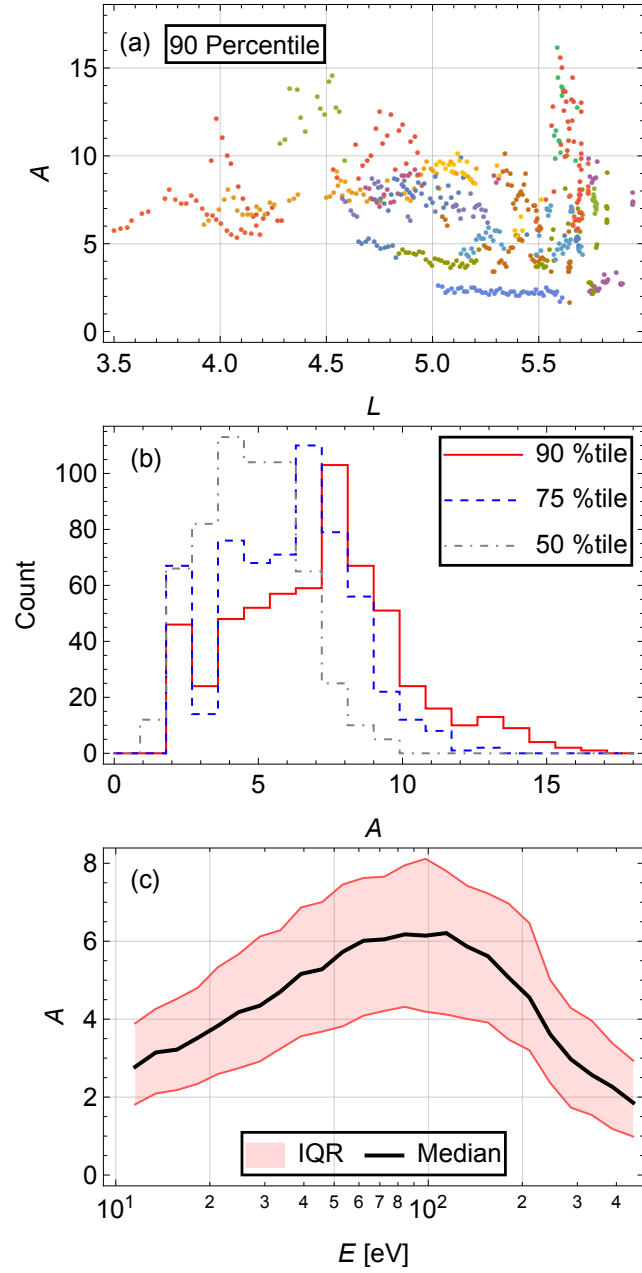


Figure 2. Low-energy (10–500 eV) proton anisotropy statistics during HFEMIC activity. (a) A versus L shell scatter plot. The dots with identical color belong in the same event. The 90th percentile of the fluxes measured at different energies is shown. (b) Histogram of A . The red solid, blue dashed, and gray dot-dashed lines correspond to the histograms of 90th, 75th, and 50th percentile values. (c) A statistical dependence of A as a function of energy. The solid black curve and the shaded region denote the median and the inter-quartile range (IQR) of A , respectively.

This is not specific to this sample case—indeed, protons in the 10–500 eV range exhibited a flux enhancement and elevated anisotropy (like Figure 1c) for all HFEMIC events. Since the pitch angle anisotropy is one of the important parameters, we extract A in this energy range and examine the correlation with the concurrent HFEMIC waves. For this, the proton flux data were averaged over a two-minute period with one-minute overlap. In the end, we obtained a two-dimensional array of A , one in time and another in energy.

Figure 2a displays a scatter plot of A versus L shell. Since A is also a function of energy, we choose the 90th percentile of the fluxes measured at different energies at each time point. The dots with identical color belong in the same event. Similar to the sample event in Figure 1, the pitch angle anisotropy is consistently large during HFEMIC activity: $A \gtrsim 2$ for all events and $A \geq 5$ for 71% of all. Notwithstanding the small number of samples, it appears that A is not strongly related to L , which appears consistent with the L dependence of the HFEMIC wave amplitude and the electron plasma-to-cyclotron frequency ratio (shown in Figures S4c and S4f). Another way to look at this may be that A has an upper bound at ~ 10 independent of L , which may be interpreted as a result of the self-regulating process by generating HFEMIC waves, as shown for typical EMIC waves (e.g., Gary & Lee, 1994; Denton et al., 1994; Yue et al., 2019). Figure 2b shows histograms of A . Clearly, the 75th percentile curve does not deviate too far from the 90th percentile curve and the majority of the median A values are greater than 2. In Figure 2c, we find that A peaks at around 100 eV, which is substantially lower than the energy ($\gtrsim 1$ keV) associated with the typical EMIC wave excitation (L. Chen, Thorne, Jordanova, Wang, et al., 2010).

From this result, we can conclude that HFEMIC waves are strongly associated with enhanced fluxes of low-energy (10–500 eV) protons with markedly elevated pitch angle anisotropy.

3.2 HFEMIC Instability Analysis

To gain further insights into the free energy source of HFEMIC waves, we carry out linear instability analysis using the low-energy proton data. Following the formulation of L. Chen et al. (2013), one can write the approximate growth rate in parallel propagation in a more data-agnostic way

$$\gamma = \frac{2\pi^2\omega_{p0}^2}{\partial D_r/\partial\omega_r} \int_{E_{\parallel}}^{\infty} \frac{dE}{2E} \left[-\frac{\omega_r}{k_{\parallel}c} \mathcal{J}_h - \sqrt{\frac{E-E_{\parallel}}{2m_p c^2}} \frac{\partial \mathcal{J}_h}{\partial \alpha} \right] \Big|_{E_{\parallel}=E_{\text{res}}}, \quad (2)$$

where ω_r is the real part of the angular wave frequency ω ; k_{\parallel} is the parallel wave number; D_r is the real part of the dispersion relation, $D(\omega, k_{\parallel}) = 0$; $\omega_{p0} = \sqrt{4\pi n_0 e^2/m_p}$ is the proton plasma frequency; $\mathcal{J}_h = m_p c^2 j_h/(n_0 c)$ is the normalized hot proton flux; and E_{res} is the parallel resonant energy. We approximate the energy integral and pitch angle derivative in the right side from $\mathcal{J}_h(E_i, \alpha_j)$ given in discrete energy and pitch angle space. The real part of wave frequency ω_r is obtained from the cold plasma dispersion relation of a proton-electron plasma. The fact that protons make up of the entire ion species is not an unreasonable assumption in the regime where the wave frequency approaches f_{cp} , but the cold plasma assumption is generally considered to be invalid in this regime where E_{res} becomes small enough that thermal protons start to resonantly interact with the waves. Nevertheless, since an elaborate fitting of model distributions like in Teng et al. (2019) is not practical for all events we have found, we use this approximate formula to get general idea of how the instability behaves qualitatively and then pick one case to carry out a more appropriate analysis.

For growth rate calculation, we average the data over the 5-minute period centered at the longest HFEMIC wave blob (see Figure 1f) and include protons only in the energy range 10–1000 eV. The number density accounted for by this population is less than

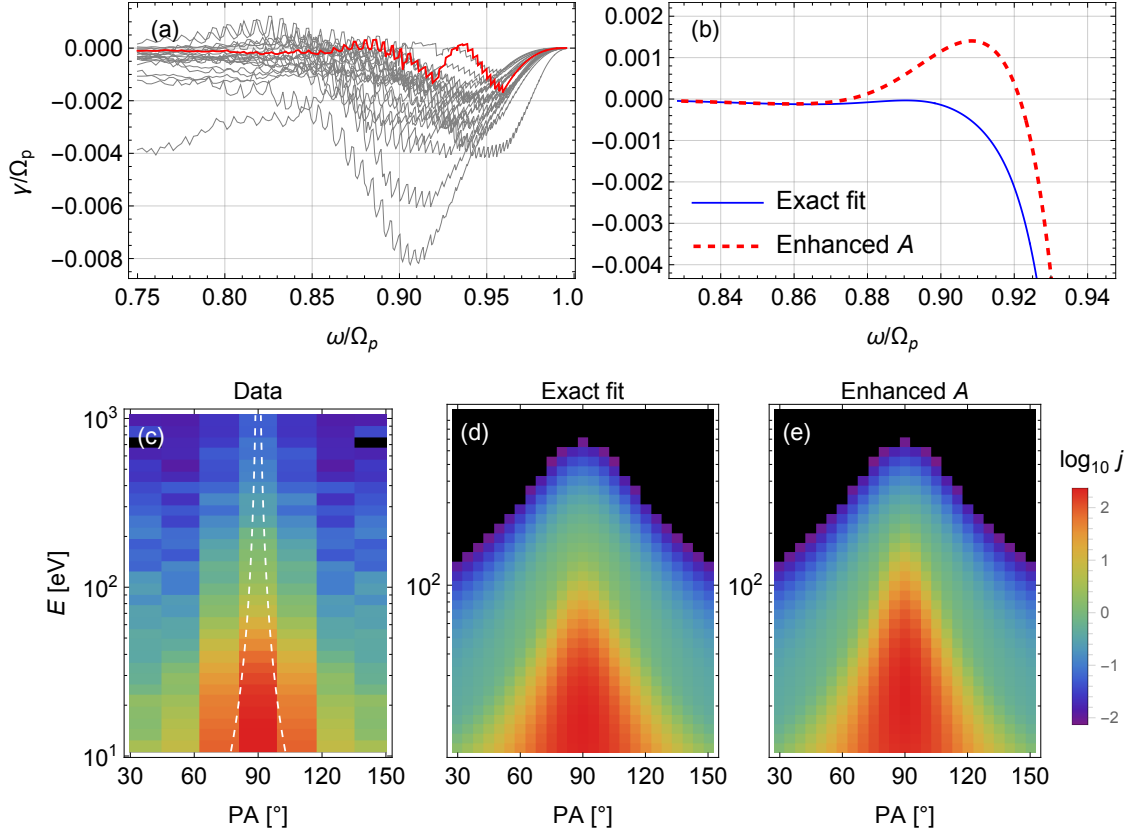


Figure 3. Summary of HFEMIC instability analysis. (a) Superposition of linear growth rates for all events calculated by Eq. (2). The event denoted with red color (detected by Probe A on August 19, 2017) is examined in detail in panels (b-e). (b) Linear growth rate from full kinetic theory at parallel propagation for the chosen event. The solid curve is the result for a model distribution fit to the data, and the dashed curve is the result for a model distribution with slightly enhanced anisotropy. (c) Proton flux as a function of energy and pitch angle from the particle data. A pair of dashed curves indicate the resonant energy corresponding to $f/f_{cp} = 0.95$. (d) Energy-pitch angle distribution of proton flux of a model proton distribution fit to the data. (e) Energy-pitch angle distribution of proton flux of a model proton distribution with slightly enhanced anisotropy.

25% (on average 15%) of the total electron density (meaning that protons of < 10 eV make up the majority) and the average temperature is ~ 50 eV. In Figure 3a, the approximate growth rates from Eq. (2) are superimposed for all HFEMIC events. The zigzag pattern in all curves is owing to \mathcal{J}_h given in discrete energy and pitch angle space with coarse resolution. No event exhibits pronounced wave growth at $f/f_{cp} \gtrsim 0.9$.

We investigate in detail the case highlighted in red which shows a local bump in the growth rate at around $f/f_{cp} = 0.93$. The corresponding energy-pitch angle distribution of proton flux is displayed in Figure 3c. Typical for all events, the flux exhibits a sharp enhancement in the vicinity of $\alpha = 90^\circ$ (which is resolved by only *three* pixels!). For simplicity, we assume a model of two bi-Maxwellian distributions to fit the data

$$f_j = \frac{n_j}{\pi^{3/2} \theta_{\parallel j} \theta_{\perp j}^2} e^{-v_{\parallel}^2 / \theta_{\parallel j}^2} e^{-v_{\perp}^2 / \theta_{\perp j}^2}. \quad (3)$$

The fitting parameters are: $n_1 = 0.2n_0$, $\theta_{\parallel 1} = 0.02v_A$, and $T_{\perp 1}/T_{\parallel 1} = 10$ for the first component, and $n_2 = 0.0045n_0$, $\theta_{\parallel 2} = 0.065v_A$, and $T_{\perp 2}/T_{\parallel 2} = 5$ for the second. The charge-neutralizing background population is assumed to have $\theta_{\parallel 3} = \theta_{\perp 3} = 0.01v_A$. (Here, $v_A = B_{eq}/\sqrt{4\pi m_p n_e}$ is the Alfvén velocity.) Figure 3d shows the model distribution which reasonably compares to the actual data. We solve the full kinetic dispersion relation at parallel propagation (e.g., L. Chen et al., 2013). The result shown in Figure 3b (blue curve) indicates no noticeable wave growth.

It is not surprising to see that the observed proton distribution is in a marginally stable state. Waves and particles self-consistently evolve and the previous analysis (Teng et al., 2019; Min et al., 2022) showed that the instability is rather weak. So, it is likely that the observed distributions have already been relaxed substantially. In fact, previous studies of EMIC waves show that almost all events fall under the instability threshold curve in anisotropy-parallel beta space (e.g., Gary & Lee, 1994; Denton et al., 1994; Noh et al., 2018; Yue et al., 2019; Jun et al., 2023). To our knowledge the instability threshold analysis in the high-frequency EMIC regime has not been done, so such a theory-observation comparison will be valuable to understand the low-energy proton to HFEMIC wave energy coupling chain. Another point worth mentioning is that the analysis here had to contend with the coarse pitch angle resolution of the particle measurement—clearly, the three-pixel coverage is not enough to resolve the sharp flux enhancement in the immediate vicinity of $\alpha = 90^\circ$ shown in Figure 3c. A pair of dashed curves in Figure 3c denotes the resonant energy, E_{res} , corresponding to $f/f_{cp} = 0.95$ (a typical peak frequency of the observed HFEMIC waves). Since Eq. (2) involves the pitch angle gradient of proton fluxes evaluated at E_{res} , the high-resolution data near $\alpha = 90^\circ$ is crucial for accurate HFEMIC instability calculation. As a demonstration of this point, if we increase the anisotropy of the first component in Figure 3d slightly (to $T_{\perp 1}/T_{\parallel 1} = 15$), HFEMIC waves can grow at $f/f_{cp} \approx 0.91$ (red dashed curve in Figure 3b), meaning that a slight increase of anisotropy renders the model distribution unstable. The corresponding energy-pitch angle distribution is shown in Figure 3e. It will be difficult to distinguish between the model distributions in Figures 3d and 3e by coarse sampling in pitch angle as in Figure 3c. Therefore, it is reasonable to conjecture that the actual pitch angle anisotropy (and its gradient at E_{res}) is greater than what is estimated in Figure 2, which of course favors the scenario that the anisotropic low-energy protons are the free energy source of HFEMIC waves.

4 MS Waves vs. Low-energy Protons

4.1 Correlation Analysis

Having shown a positive correlation between HFEMIC occurrence and the enhancement of low-energy proton anisotropy, we now turn to the correlation analysis between the low-energy proton enhancement and MS waves. Since the MS wave-driven heating

occurs preferentially in the direction perpendicular to the magnetic field, we once again utilize the anisotropy parameter of Eq. (1) of protons. For MS waves, the key parameters are the wave amplitude and harmonic number (assuming that wave normal angles are quasi-perpendicular).

For statistical analysis, we identify MS waves from the WFR data based on the criteria: wave normal angle greater than 70° , ellipticity within ± 0.25 (i.e., linear polarization), and harmonic frequency $f \leq 42f_{cp}$. The white contour in Figure 1b demarcates the identified MS waves based on these criteria. Even though no minimum harmonic frequency is imposed, all but one event show MS waves at $f \gtrsim f_{cp}$. It should be noted that the WFR data can miss very low-harmonic MS waves due to the low sensitivity and coarse frequency resolution in the low-frequency regime. Ma, Li, Bortnik, et al. (2019) performed a survey using both fluxgate and search coil magnetometers of Van Allen Probes and found that low-harmonic MS waves can have high power at $L > 4$ outside the plasma-pause. Furthermore, Teng et al. (2021) showed that even the fluxgate magnetometer on board Van Allen Probes can miss some low-harmonic MS waves with weak magnetic field intensity because of relatively high measurement thresholds. After checking the fluxgate magnetic field and EFW data, we found three events of low-harmonic MS waves which show up only in the EFW data. (Due to the sampling limit of EFW, only the first five harmonic modes can be examined.) Their low occurrence rate (and the fact that these waves are absent from the fluxgate data) suggests that the WFR data alone should be sufficient for the statistical analysis below.

Similarly, we apply a set of criteria to systematically select the enhanced anisotropy of low-energy protons: Guided by Figure 2a, we choose an anisotropy threshold $A > 3$ in the 10–500 eV range. In the end, two out of 26 events did not meet this minimum requirement. The white contour in Figure 1d indicates the identified region of enhanced A . Although visually the region of enhanced anisotropy extends nearly to the end of the plot, the later half of the region is not selected because of the anisotropy being lower than the threshold. In fact, the two events that did not meet the threshold still exhibit a clear 90° -peaked pitch angle distribution. In that sense, the anisotropy threshold $A = 3$ is a conservative choice. (A threshold value of $A = 4$ does not change the fundamental result here, only reducing the number of data points.)

Figure 4a shows a relation between MS wave amplitude and harmonic number. Despite the data scatter, there is a noticeable inverse relationship: The smaller the harmonic number is, the larger the wave amplitude tends to get (e.g., Ma, Li, Bortnik, et al., 2019). Also, there are a lot more samples at low harmonic frequencies, which can be understood by the fact that MS waves with larger amplitude are more easily detectable. Figure 4b plots MS wave amplitude against magnetic latitude. The wave occurrence is clearly confined to within $\pm 5^\circ$ latitude and the amplitude maximizes at the equator (e.g., Boardman et al., 2016). Certainly, the inverse relationship and latitudinal confinement of the MS wave occurrence in Figure 4 are the typical features expected from MS waves.

Figure 5a displays for each event the fraction of MS wave occurrence over the duration of enhanced proton anisotropy. A 100% means that MS waves occurred for the entire duration of enhanced anisotropy. So, for 15 out of 24 events, MS waves lasted as long as (and perhaps longer than) the anisotropy enhancement did. Even for those below 100%, the coverage is greater than 50% (with one exception having a 25% coverage).

However, the good MS wave coverage does not necessarily mean the causal relationship. Figure 5b shows a relation between 90th percentile A values (A_{90th} calculated in the same way as in Figure 2a) and MS wave amplitude. Since there are events with fractional MS wave coverage, there are points with no corresponding MS wave power. These are denoted by the cross symbols in the left side and make up of 11% of data points in the figure. (Despite no concurrent MS waves, they still have large A_{90th} values (~ 5) associated with them.) For those that do have finite MS wave power associated them,

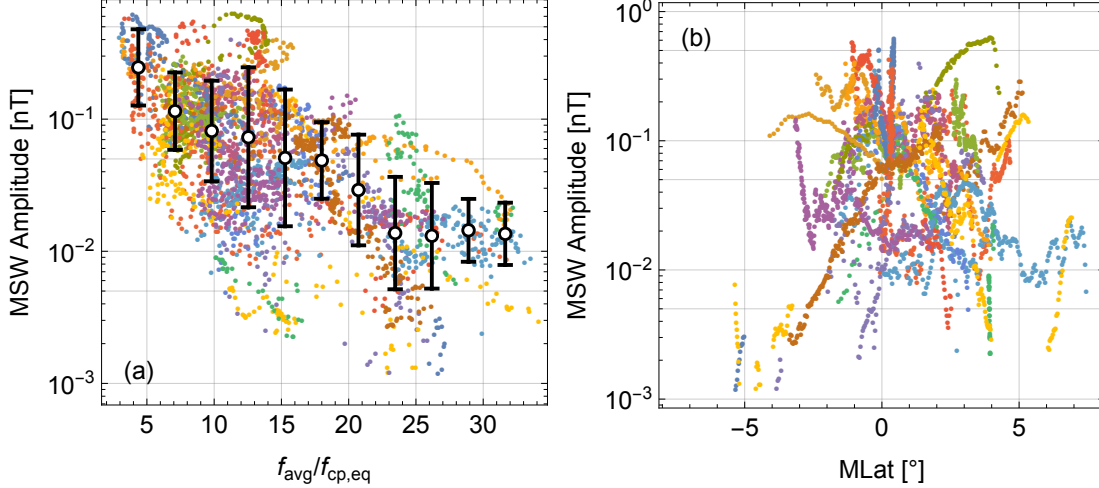


Figure 4. (a) MS wave amplitude versus power-weighted average frequency, f_{avg} , normalized by f_{cp} . The dots and vertical bars denote the mean and one standard deviation, respectively. (b) MS wave amplitude versus magnetic latitude. The dots with the same color belong in the same event.

the correlation between A_{90th} and MS wave amplitude is not so clear. If the low-energy proton heating (preferentially in the perpendicular direction) is driven by the concurrent MS waves, one would expect to see a positive correlation between A_{90th} and MS wave amplitude. Although the mean value (denoted by open circles) does seem to show a mild increase with MS wave amplitude in the weak-amplitude region, the trend flattens out at the large amplitude region (where we expect to see an efficient acceleration by MS waves and thus a more anisotropic distribution). In general, it is quite difficult to make out a clear trend because of the large data scatter. Similarly, Figure 5c shows a relation between A_{90th} and power-averaged MS wave harmonic number (f_{avg}/f_{cp}). No particular dependence stands out in this case, either. Considering that the harmonic number is inversely related to MS wave amplitude in Figure 4a, a decreasing trend should be expected here. In that regard, the increasing trend shown in the weak-amplitude region in Figure 5b may not be related to the MS wave-driven heating at all. Figures 5d and 5e show correlations of the average proton energy normalized by the Alfvén energy (E_{avg}/E_A) with the MS wave amplitude and harmonic number, respectively. We use the normalized energy because in linear theory the energy of protons in resonance with MS waves are scaled by E_A (see, e.g., Horne et al., 2000). Similar to the previous two plots, it is hard to glean any meaningful statistical correlations due to the large data scatter. Interestingly, the trend of E_{avg}/E_A in Figure 5d appears to be quite similar to the trend shown in Figure 5b.

In summary, despite the decent coverage by MS waves during the period of enhanced anisotropy (and fluxes) of low-energy protons, the lack of correlations between the key parameters that are relevant to MS wave-driven heating suggests that statistically the low-energy proton enhancement driven by concurrent MS waves is inconclusive.

4.2 Quasilinear Diffusion

According to Min et al. (2022), quasilinear theory does not seem to favor efficient heating of low-energy protons, either. Considering near-equatorially mirroring protons interacting with MS waves at quasi-perpendicular propagation, the momentum diffusion

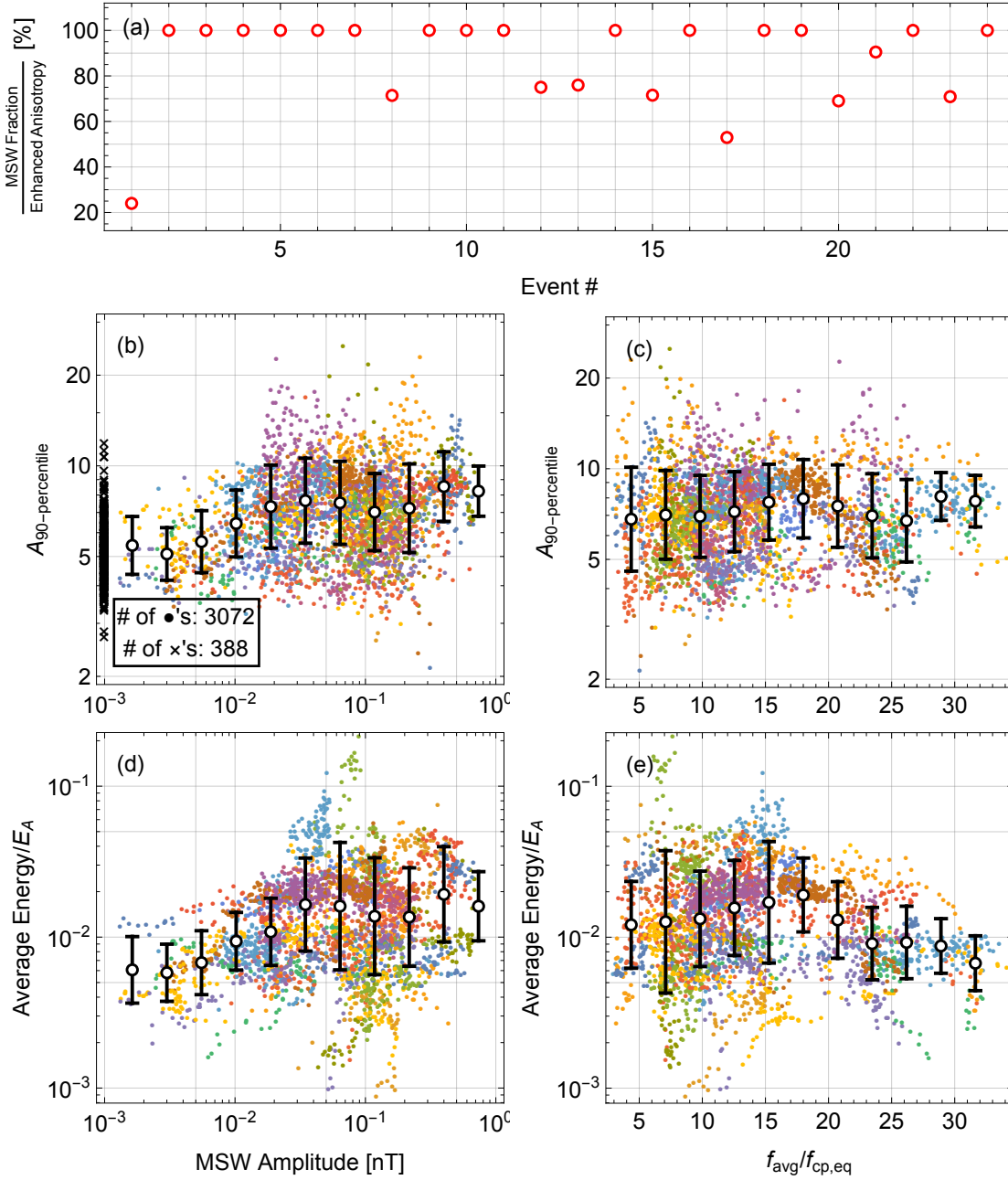


Figure 5. Correlation analysis between MS waves and low-energy protons. (a) Fraction of MS wave occurrence over the duration of enhanced proton anisotropy. (b) 90th percentile A (A_{90th}) versus MS wave amplitude. The data points with no MS wave power (for those events having less than a 100% coverage) are shown with the cross symbols on the left side. The number of data points with finite MS wave power is about 3100 and the number with no MS wave power is about 400. (c) A_{90th} versus f_{avg}/f_{cp} , where f_{avg} is the power-weighted average MS wave frequency. (d) Average proton energy normalized by the Alfvén energy (E_{avg}/E_A) versus MS wave amplitude. (e) E_{avg}/E_A versus f_{avg}/f_{cp} . In panels (b-e), the open circles and vertical bars correspond to the mean and one standard deviation, respectively.

coefficient can be written as (Min & Liu, 2021)

$$D_{\perp\perp} = \pi \Omega_p^2 \sum_n \frac{\omega^2}{k_{\perp}^2} \frac{W_B(\omega)}{B_{eq}^2} \frac{n^2 \Omega_p^2}{k_{\perp}^2 v_{\perp}^2} J_n^2 \left(\frac{k_{\perp} v_{\perp}}{\Omega_p} \right), \quad (4)$$

where $\Omega_p = 2\pi f_{cp}$, k_{\perp} is the perpendicular wave number, v_{\perp} is the perpendicular component of proton velocity, n is the resonance order, $J_n(x)$ is the Bessel function of the first kind, and $W_B(\omega)$ is the magnetic field power spectral density. Figure 6a plots $D_{\perp\perp}$ as a function of E/E_A , corresponding to $n = 2, 3, 5$, and 10. For all curves, the momentum diffusion coefficient peaks at $E \gtrsim E_A$ and monotonically decreases with decreasing energy. In addition, the smaller the harmonic number gets, the slower the decreasing rate becomes. Therefore, it is with the small harmonic MS waves that lead to a maximal scattering rate in the low-energy regime. As we will see, $E_A \gtrsim 1$ keV in our events. So, it is only the first few harmonic modes that will be most effective in the low-energy (~ 10 – 100 eV) proton heating.

For qualitative analysis, we calculate the momentum diffusion coefficient of equatorially mirroring protons using the MS wave power spectra identified in the previous subsection, assuming that MS waves propagate strictly perpendicular to the background magnetic field. Although the latter assumption is not valid in general, Min et al. (2022) showed that Eq. (4) can qualitatively represent the overall trend of the bounce-averaged diffusion rate of near-equatorially mirroring protons (see also Supporting Information S2 and S5). In Figure 6b, we show the ratio of $D_{\perp\perp}$ at $E = 10$ and 100 eV (black and red dots, respectively) to the maximum of $D_{\perp\perp}$ at each time bin, plotted against f_{avg}/f_{cp} . The horizontal dashed line is drawn at 10^{-3} , meaning that the diffusion rate is three orders of magnitude smaller than the maximum. The majority of points are below the 10^{-3} mark. Furthermore, there is an inverse relationship between the ratio and the harmonic number, and the diffusion rate gets larger for more energetic protons (red versus black dots). In Figure 6c, we show the energy at which $D_{\perp\perp}$ maximizes versus the Alfvén energy. The peak energy is typically greater than E_A (and within a factor of two). This is essentially controlled by the Bessel function term in Eq. (4) and the dispersion relation approximately given by $\omega \sim v_A k_{\perp}$ (L. Chen, Thorne, Jordanova, & Horne, 2010). We emphasize that even though WFR can miss very low-harmonic MS waves, the number of such events identified from the fluxgate and EFW data is actually small.

5 Summary and Discussion

We carried out a comprehensive statistical analysis using the Van Allen Probes data to provide deeper insights into the energy coupling from MS waves to HFEMIC waves through the heating of low-energy protons. We identified 26 HFEMIC wave events from both spacecraft for the entire mission period and performed correlation analyses among the key parameters relevant to diagnose the suggested chain of energy flow. Our findings can be summarized as follows:

1. For all events, HFEMIC waves are strongly associated with enhanced fluxes and elevated pitch angle anisotropy of low-energy (10–500 eV) protons. The pitch angle anisotropy during HFEMIC activity is much larger than the threshold value ($A \sim 1$) needed to excite typical EMIC waves and statistically peaks at energy ~ 100 eV. The linear instability calculation indicated that the observed low-energy protons are marginally stable to HFEMIC waves. However, part of the reason has to do with the low pitch angle resolution of the proton flux data, which can smooth out the rapid variation of proton flux in the vicinity of 90° pitch angle and thus underestimate the actual pitch angle anisotropy and its gradient at such a low resonant energy.
2. Although MS waves and enhanced low-energy protons occurred semi-concurrently, the lack of correlations between the key parameters that are relevant to MS wave-

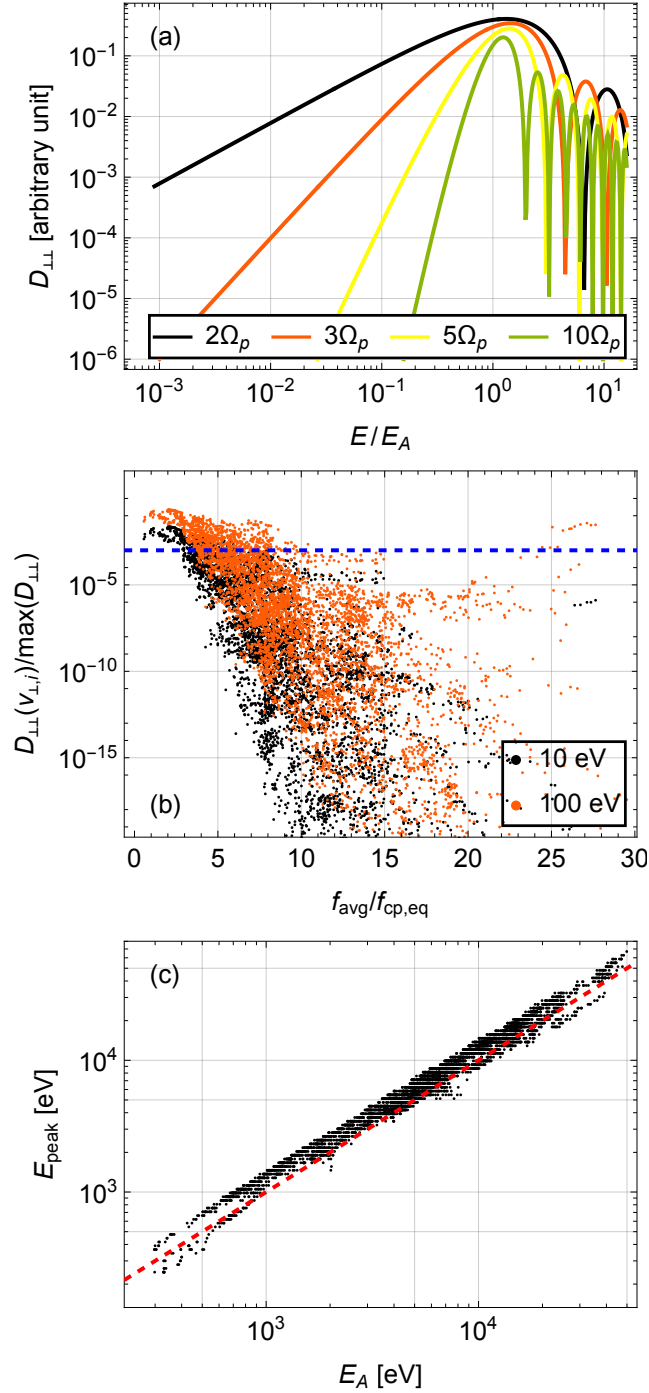


Figure 6. (a) Momentum diffusion coefficient, $D_{\perp\perp}$, of Eq. (4) corresponding to the harmonic modes, $n = 2, 3, 5$, and 10 . The energy on the horizontal axis is normalized by the Alfvén energy, E_A . (b) Ratio of $D_{\perp\perp}$ at 10 (black) and 100 (red) eV to the maximum of $D_{\perp\perp}$, calculated using the observed MS wave power spectra. (c) Energy at the maximum diffusion coefficient, E_{max} , versus Alfvén energy, E_A .

driven heating suggests that statistically the role of MS waves as the driver of anisotropic low-energy protons is questionable. This result is given support by the quasilinear analysis where the momentum diffusion rate maximizes at energy slightly larger than the Alfvén energy (which is $\gtrsim 1$ keV) and the scattering efficiency drops precipitously with a decreasing energy. Although the resonant interactions with low-harmonic MS waves can elevate the scattering efficiency and we indeed found several events of low-harmonic MS waves, for most of the cases the diffusion rate at 10–100 eV is several orders of magnitude lower compared to the maximum rate.

All things considered, it is not unreasonable to believe that the low-energy protons with enhanced anisotropy are the free energy source of HFEMIC waves, but it is comparatively hard to justify the resonant interactions with MS waves as the (primary) source of the enhanced low-energy protons. It is not to say that the results of Asamura et al. (2021), which is based on a quantitative analysis, are erroneous, but it makes more sense, in general, to view the semi-concurrent MS waves and enhanced low-energy protons as having a common driver, rather than being causally related. Having said that, we cannot rule out any non-resonant, nonlinear effect we have neglected here. Theoretical and particle-in-cell simulation studies (Artemyev et al., 2017; Sun et al., 2017; Min et al., 2022) highlighted that such an effect may be important. However, at this point more quantitative theories need to be materialized and even then they must reconcile the observational results presented in Figure 5.

Other possibilities not considered here may include the spatial effect: The low-energy protons could have been energized at earlier local time where there were strong MS wave activity and then drifted to where the measurement was made. In this way, the weak correlation between MS waves and low-energy protons could be explained if the measurement was made far from the MS wave source region. According to Ma, Li, Bortnik, et al. (2019, Figure 4), the occurrence of low-harmonic MS waves appears to peak slightly ahead of our HFEMIC events (Figure S4a), when AE^* (defined as the maximum geomagnetic auroral electrojet (AE) index value in the previous 3 hr) is larger than 500 nT (i.e., moderate substorm activity). However, although we did not examine the geomagnetic conditions, Jun et al. (2021, 2023) reported that H-band EMIC waves with frequencies from 0.23 to $0.95f_{cp}$ tend to occur during relatively quiet geomagnetic conditions, which is not in favor of this scenario.

On the other hand, MS waves and low-energy protons need not be causally related to each other just because they appear concurrently. Considering how frequently pancake distributions of low-energy protons are found with MS waves shown in a recent study (Wu et al., 2022) (although one should be careful in the interpretation of Wu et al. (2022, Figure 4) because of the different normalization), it is possible that they have a common driver. Joseph et al. (2022) recently proposed an alternative explanation for the origin of low-energy, anisotropic protons (see Figure 6 therein). In this scenario, the polar wind outflow is intensified under geomagnetically disturbed conditions. Depending on the strength of the southward interplanetary magnetic field, the entry point of the polar wind can be closer to, or far away from, the Earth. As the polar wind plasma particles get injected towards the Earth, they gain energy adiabatically, preferentially in the direction perpendicular to the background magnetic field. The plasma particles whose entry point is far away from the Earth can attain ring current energies, and those that have entered closer to the Earth becomes the warm plasma cloak with a high anisotropy. Thus, the former population can be the source for MS waves and the latter becomes the source of HFEMIC waves. In that regard, this scenario may be able to explain the semi-concurrent MS waves and low-energy anisotropic proton population. On the other hand, not all HFEMIC waves seem to occur during geomagnetically disturbed times, as reported by Jun et al. (2021, 2023). Nevertheless, this is an interesting idea that warrants further investigation.

Enhanced solar wind dynamic pressure is also known to cause proton temperature anisotropy on the dayside of the magnetosphere as a result of adiabatic heating (Anderson & Hamilton, 1993; McCollough et al., 2010). Interestingly, this is also the region where most of our HFEMIC events were found. However, this mechanism is unlikely to explain our low-energy proton observations because we would have seen an enhancement in anisotropy in all energies consistently and an elevated anisotropy alone is not sufficient to excite MS waves.

The warm plasma population is indispensable to the dynamics in the magnetosphere. Therefore, revealing the processes involved in the perpendicular acceleration of low-energy protons is important for quantifying the cross-scale and cross-energy coupling.

6 Open Research

The authors acknowledge the EMFISIS data obtained from <https://emfisis.physics.uiowa.edu/Flight/>, the HOPE data obtained from <http://www.rbsp-ect.lanl.gov/data-pub/>, and the EFW data from <http://www.space.umn.edu/data/rbsp/>.

Acknowledgments

K.M. graciously acknowledges the support from the National Research Foundation of Korea (NRF) grant funded by the Korea government (MSIT) (No. 2020R1C1C100999612). Q.M. would like to acknowledge the NASA grant 80NSSC20K0196, NSF grant AGS-2225445, and the support from NSF Geospace Environment Modeling focus group “Self-Consistent Inner Magnetospheric Modeling.”

References

- Anderson, B. J., & Hamilton, D. C. (1993, July). Electromagnetic ion cyclotron waves stimulated by modest magnetospheric compressions. *J. Geophys. Res.*, *98*(A7), 11369-11382. doi: 10.1029/93JA00605
- Artemyev, A. V., Mourenas, D., Agapitov, O. V., & Blum, L. (2017, February). Transverse eV ion heating by random electric field fluctuations in the plasmasphere. *Physics of Plasmas*, *24*(2), 022903. doi: 10.1063/1.4976713
- Asamura, K., Shoji, M., Miyoshi, Y., Kasahara, Y., Kasaba, Y., Kumamoto, A., ... Shinohara, I. (2021, December). Cross-Energy Couplings from Magnetosonic Waves to Electromagnetic Ion Cyclotron Waves through Cold Ion Heating inside the Plasmasphere. *Physical Review Letters*, *127*(24), 245101. doi: 10.1103/PhysRevLett.127.245101
- Boardson, S. A., Hospodarsky, G. B., Kletzing, C. A., Engebretson, M. J., Pfaff, R. F., Wygant, J. R., ... De Pascuale, S. (2016, April). Survey of the frequency dependent latitudinal distribution of the fast magnetosonic wave mode from Van Allen Probes Electric and Magnetic Field Instrument and Integrated Science waveform receiver plasma wave analysis. *Journal of Geophysical Research (Space Physics)*, *121*, 2902-2921. doi: 10.1002/2015JA021844
- Breneman, A. W., Wygant, J. R., Tian, S., Cattell, C. A., Thaller, S. A., Goetz, K., ... Millan, R. (2022, December). The Van Allen Probes Electric Field and Waves Instrument: Science Results, Measurements, and Access to Data. *Space Sci. Rev.*, *218*(8), 69. doi: 10.1007/s11214-022-00934-y
- Chen, L., Thorne, R. M., Jordanova, V. K., & Horne, R. B. (2010, November). Global simulation of magnetosonic wave instability in the storm time magnetosphere. *Journal of Geophysical Research (Space Physics)*, *115*(A11), A11222. doi: 10.1029/2010JA015707
- Chen, L., Thorne, R. M., Jordanova, V. K., Wang, C.-P., Gkioulidou, M., Lyons, L., & Horne, R. B. (2010, July). Global simulation of EMIC wave excitation

- during the 21 April 2001 storm from coupled RCM-RAM-HOTRAY modeling. *Journal of Geophysical Research (Space Physics)*, *115*(A7), A07209. doi: 10.1029/2009JA015075
- Chen, L., Thorne, R. M., Shprits, Y., & Ni, B. (2013, May). An improved dispersion relation for parallel propagating electromagnetic waves in warm plasmas: Application to electron scattering. *Journal of Geophysical Research (Space Physics)*, *118*(5), 2185-2195. doi: 10.1002/jgra.50260
- Chen, M. W., Roeder, J. L., Fennell, J. F., Lyons, L. R., Lambour, R. L., & Schulz, M. (1999, August). Proton ring current pitch angle distributions: Comparison of simulations with CRRES observations. *J. Geophys. Res.*, *104*(A8), 17379-17390. doi: 10.1029/1999JA900142
- Denton, R. E., Gary, S. P., Anderson, B. J., Fuselier, S. A., & Hudson, M. K. (1994, April). Low-frequency magnetic fluctuation spectra in the magnetosheath and plasma depletion layer. *J. Geophys. Res.*, *99*(A4), 5893-5902. doi: 10.1029/93JA02729
- Ferradas, C. P., Boardsen, S. A., Fok, M. C., Buzulukova, N., Reeves, G. D., & Larsen, B. A. (2021, March). Observations of Density Cavities and Associated Warm Ion Flux Enhancements in the Inner Magnetosphere. *Journal of Geophysical Research (Space Physics)*, *126*(3), e28326. doi: 10.1029/2020JA028326
- Funsten, H. O., Skoug, R. M., Guthrie, A. A., MacDonald, E. A., Baldonado, J. R., Harper, R. W., ... Chen, J. (2013, November). Helium, Oxygen, Proton, and Electron (HOPE) Mass Spectrometer for the Radiation Belt Storm Probes Mission. *Space Science Reviews*, *179*(1-4), 423-484. doi: 10.1007/s11214-013-9968-7
- Gary, S. P., & Lee, M. A. (1994, June). The ion cyclotron anisotropy instability and the inverse correlation between proton anisotropy and proton beta. *J. Geophys. Res.*, *99*(A6), 11297-11302. doi: 10.1029/94JA00253
- Hill, S., Buzulukova, N., Boardsen, S., & Fok, M. C. (2020, August). Local Heating of Oxygen Ions in the Presence of Magnetosonic Waves: Possible Source for the Warm Plasma Cloak? *Journal of Geophysical Research (Space Physics)*, *125*(8), e27210. doi: 10.1029/2019JA027210
- Horne, R. B., Wheeler, G. V., & Alleyne, H. S. C. K. (2000, December). Proton and electron heating by radially propagating fast magnetosonic waves. *J. Geophys. Res.*, *105*, 27597-27610. doi: 10.1029/2000JA000018
- Joseph, J., Jaynes, A. N., Ma, Q., Hartley, D. P., Usanova, M. E., & Li, W. (2022, November). Relation between Magnetosonic Waves and Pitch Angle Anisotropy of Warm Protons. *Frontiers in Astronomy and Space Sciences*, *9*, 378. doi: 10.3389/fspas.2022.1035563
- Jun, C.-W., Miyoshi, Y., Kurita, S., Yue, C., Bortnik, J., Lyons, L., ... Shinohara, I. (2021, June). The Characteristics of EMIC Waves in the Magnetosphere Based on the Van Allen Probes and Arase Observations. *Journal of Geophysical Research (Space Physics)*, *126*(6), e29001. doi: 10.1029/2020JA029001
- Jun, C. W., Miyoshi, Y., Nakamura, S., Shoji, M., Kitahara, M., Hori, T., ... Keika, K. (2023, June). Statistical Study of EMIC Waves and Related Proton Distributions Observed by the Arase Satellite. *Journal of Geophysical Research (Space Physics)*, *128*(6), e2022JA031131. doi: 10.1029/2022JA031131
- Kennel, C. F., & Petschek, H. E. (1966, January). Limit on Stably Trapped Particle Fluxes. *J. Geophys. Res.*, *71*, 1. doi: 10.1029/JZ071i001p00001
- Kletzing, C. A., Bortnik, J., Hospodarsky, G., Kurth, W. S., Santolik, O., Smith, C. W., ... Sen Gupta, A. (2023, June). The Electric and Magnetic Fields Instrument Suite and Integrated Science (EMFISIS): Science, Data, and Usage Best Practices. *Space Science Reviews*, *219*(4), 28. doi: 10.1007/s11214-023-00973-z
- Kletzing, C. A., Kurth, W. S., Acuna, M., MacDowall, R. J., Torbert, R. B.,

- Averkamp, T., ... Tyler, J. (2013, November). The Electric and Magnetic Field Instrument Suite and Integrated Science (EMFISIS) on RBSP. *Space Sci. Rev.*, 179(1-4), 127-181. doi: 10.1007/s11214-013-9993-6
- Kurth, W. S., De Pascuale, S., Faden, J. B., Kletzing, C. A., Hospodarsky, G. B., Thaller, S., & Wygant, J. R. (2015, February). Electron densities inferred from plasma wave spectra obtained by the Waves instrument on Van Allen Probes. *Journal of Geophysical Research (Space Physics)*, 120(2), 904-914. doi: 10.1002/2014JA020857
- Li, W., Thorne, R. M., Angelopoulos, V., Bonnell, J. W., McFadden, J. P., Carlson, C. W., ... Auster, H. U. (2009, February). Evaluation of whistler-mode chorus intensification on the nightside during an injection event observed on the THEMIS spacecraft. *Journal of Geophysical Research (Space Physics)*, 114(8), A00C14. doi: 10.1029/2008JA013554
- Ma, Q., Li, W., Bortnik, J., Kletzing, C. A., Kurth, W. S., Hospodarsky, G. B., & Wygant, J. R. (2019, December). Global Survey and Empirical Model of Fast Magnetosonic Waves Over Their Full Frequency Range in Earth's Inner Magnetosphere. *Journal of Geophysical Research (Space Physics)*, 124(12), 10,270-10,282. doi: 10.1029/2019JA027407
- Ma, Q., Li, W., Yue, C., Thorne, R. M., Bortnik, J., Kletzing, C. A., ... Spence, H. E. (2019, June). Ion Heating by Electromagnetic Ion Cyclotron Waves and Magnetosonic Waves in the Earth's Inner Magnetosphere. *Geophys. Res. Lett.*, 46(12), 6258-6267. doi: 10.1029/2019GL083513
- Mauk, B. H., Fox, N. J., Kanekal, S. G., Kessel, R. L., Sibeck, D. G., & Ukhorskiy, A. (2013, November). Science Objectives and Rationale for the Radiation Belt Storm Probes Mission. *Space Science Reviews*, 179(1-4), 3-27. doi: 10.1007/s11214-012-9908-y
- McCollough, J. P., Elkington, S. R., Usanova, M. E., Mann, I. R., Baker, D. N., & Kale, Z. C. (2010, October). Physical mechanisms of compressional EMIC wave growth. *Journal of Geophysical Research (Space Physics)*, 115(A10), A10214. doi: 10.1029/2010JA015393
- Min, K., Kim, J., Ma, Q., Jun, C.-W., & Liu, K. (2022, January). Unusual high frequency EMIC waves: Detailed analysis of EMIC wave excitation and energy coupling between EMIC and magnetosonic waves. *Advances in Space Research*, 69(1), 35-47. doi: 10.1016/j.asr.2021.07.039
- Min, K., & Liu, K. (2021, December). Quasilinear Diffusion of Protons by Equatorial Magnetosonic Waves at Quasi-Perpendicular Propagation: Comparison With the Test-Particle Approach. *Journal of Geophysical Research (Space Physics)*, 126(12), e29767. doi: 10.1029/2021JA029767
- Miyoshi, Y., Shinohara, I., Takashima, T., Asamura, K., Higashio, N., Mitani, T., ... Seki, K. (2018, June). Geospace exploration project ERG. *Earth, Planets and Space*, 70(1), 101. doi: 10.1186/s40623-018-0862-0
- Noh, S.-J., Lee, D.-Y., Choi, C.-R., Kim, H., & Skoug, R. (2018, August). Test of Ion Cyclotron Resonance Instability Using Proton Distributions Obtained From Van Allen Probe-A Observations. *Journal of Geophysical Research (Space Physics)*, 123(8), 6591-6610. doi: 10.1029/2018JA025385
- Spence, H. E., Reeves, G. D., Baker, D. N., Blake, J. B., Bolton, M., Bourdarie, S., ... Thorne, R. M. (2013, November). Science Goals and Overview of the Radiation Belt Storm Probes (RBSP) Energetic Particle, Composition, and Thermal Plasma (ECT) Suite on NASA's Van Allen Probes Mission. *Space Science Reviews*, 179(1-4), 311-336. doi: 10.1007/s11214-013-0007-5
- Sun, J., Gao, X., Lu, Q., Chen, L., Liu, X., Wang, X., ... Wang, S. (2017, May). Spectral properties and associated plasma energization by magnetosonic waves in the Earth's magnetosphere: Particle-in-cell simulations. *Journal of Geophysical Research (Space Physics)*, 122, 5377-5390. doi: 10.1002/2017JA024027
- Teng, S., Li, W., Tao, X., Ma, Q., Wu, Y., Capannolo, L., ... Gan, L. (2019,

- December). Generation and Characteristics of Unusual High Frequency
 EMIC Waves. *Geophys. Res. Lett.*, 46(24), 14,230-14,238. doi: 10.1029/
 2019GL085220
- Teng, S., Liu, N., Ma, Q., & Tao, X. (2021, April). Characteristics of Low Harmonic
 Magnetosonic Waves in the Earth's Inner Magnetosphere. *Geophys. Res. Lett.*,
 48(8), e93119. doi: 10.1029/2021GL093119
- Usanova, M. E., Drozdov, A., Orlova, K., Mann, I. R., Shprits, Y., Robertson,
 M. T., ... Wygant, J. (2014, March). Effect of EMIC waves on rela-
 tivistic and ultrarelativistic electron populations: Ground-based and Van
 Allen Probes observations. *Geophys. Res. Lett.*, 41(5), 1375-1381. doi:
 10.1002/2013GL059024
- Wu, Z., Teng, S., Ma, Q., & Tao, X. (2022, May). A Statistical Study of Pan-
 cake Pitch Angle Distribution of Low-Energy Protons and Their Correlation
 With Magnetosonic Waves. *Journal of Geophysical Research (Space Physics)*,
 127(5), e30174. doi: 10.1029/2021JA030174
- Wygant, J. R., Bonnell, J. W., Goetz, K., Ergun, R. E., Mozer, F. S., Bale, S. D.,
 ... Tao, J. B. (2013, November). The Electric Field and Waves Instruments on
 the Radiation Belt Storm Probes Mission. *Space Sci. Rev.*, 179(1-4), 183-220.
 doi: 10.1007/s11214-013-0013-7
- Yuan, Z., Yu, X., Huang, S., Qiao, Z., Yao, F., & Funsten, H. O. (2018, February).
 Cold Ion Heating by Magnetosonic Waves in a Density Cavity of the Plasma-
 sphere. *Journal of Geophysical Research (Space Physics)*, 123(2), 1242-1250.
 doi: 10.1002/2017JA024919
- Yue, C., Jun, C.-W., Bortnik, J., An, X., Ma, Q., Reeves, G. D., ... Kletzing, C. A.
 (2019, April). The Relationship Between EMIC Wave Properties and Proton
 Distributions Based on Van Allen Probes Observations. *Geophys. Res. Lett.*,
 46(8), 4070-4078. doi: 10.1029/2019GL082633